Received: 5 January 2018 | Revised: 31 January 2018 | Accepted: 3 February 2018

DOI: 10.1002/aoc.4337

WILEY Applied Organometallic Chemistry

FULL PAPER

Mononuclear Co(III), Ni(II) and Cu(II) complexes of tridentate di-*tert*-butylphenylhydrazone: Synthesis, characterization, X-ray crystal structures, Hirshfeld surface analysis, molecular docking and *in vivo* anti-inflammatory activity

Geeta H. Chimmalagi[1] | Umashri Kendur[1] | Sunil M. Patil[1] | Kalagouda B. Gudasi[1] | Christopher S. Frampton[2] | Mahantesh B. Budri[1] | Chandrashekhar V. Mangannavar[3] | Iranna S. Muchchandi[3]

[1] Department of Chemistry, Karnatak University, Dharwad-580003, Karnataka, India

[2] Institute of Materials and Manufacturing, Wolfson Centre for Materials Processing, Brunel University, London, UK

[3] H. S. K. College of Pharmacy, Bagalkot-587101, Karnataka, India

Correspondence
Kalagouda B. Gudasi, Department of Chemistry, Karnatak University, Dharwad – 580003, Karnataka, India.
Email: kbgudasi@gmail.com

Funding information
UGC, UPE-FAR-I Program, Grant/Award Number: 14-3/2012

A new hydrazone (LH_2) derived from the condensation of 2-(4-fluorobenzamido) benzohydrazide with 3,5-di-*tert*-butyl-2-hydroxybenzaldehyde was used to synthesize Co(III), Ni(II) and Cu(II) complexes. These were characterized using various physicochemical, thermal, spectroscopic and single-crystal X-ray diffraction techniques. All the complexes crystallize in a monoclinic crystal system with $P2_1/n$ space group and $Z = 4$. Structural studies of $[Co(L)(LH)]\cdot H_2O$ indicate the presence of both amido and imidol tautomeric forms of the ligand, resulting in a distorted octahedral geometry around the Co(III) ion. On the other hand, in the [Ni(L)(DMF)] and $[Cu(L)(H_2O)]$ complexes, the ligand coordinates to the metal through imidol form resulting in distorted square planar geometry, in which the fourth position is occupied by the oxygen of coordinated DMF in [Ni(L)(DMF)] and by a water molecule in $[Cu(L)(H_2O)]$. Hirshfeld surface calculations were performed to explore hydrogen bonding and C—H···π interactions. Molecular docking studies were carried out to study the interaction between the synthesized compounds and proteins (cyclooxygenase-2 and 5-lipoxygenase). The complexes along with the parent ligand were screened for their *in vivo* anti-inflammatory activity, using the carrageenan-induced rat paw oedema method. The complexes show significant anti-inflammatory potencies.

KEYWORDS
anti-inflammatory activity, Hirshfeld surface analysis, molecular docking, transition metal complexes, X-ray diffraction study

1 | INTRODUCTION

Over the past several decades, inflammation has been renowned as a devastating burden and the prime basis of various inflammatory-related diseases. The metabolites of arachidonic acid (AA) such as prostaglandins and leukotrienes (generated by cyclooxygenase (COX) and 5-lipoxygenase (5-LOX) enzymatic pathways, respectively) have been associated as mediators in an assortment of diseases, including asthma, inflammation

and cell proliferation.[1,2] Classical non-steroidal anti-inflammatory drugs (NSAIDs) which are non-selective COX inhibitors have been widely used for the treatment of inflammation.[3,4] In the treatment of arthritis, NSAIDs offer an efficient treatment, but safety is significantly compromised, mainly due to an up-regulation of the AA metabolism by the 5-LOX pathway, increasing the formation of pro-inflammatory leukotrienes and contributing to gastrointestinal ulcerations and atherosclerosis.[5] Since the selective inhibition of one pathway in the AA cascade appears to cause undesired effects, more recently several clinically effective NSAIDs have been structurally modified to yield potent dual COX-2/5-LOX inhibitors.[6,7]

Aroylhydrazones are an extremely versatile group of compounds in the family of Schiff bases. Transition metal complexes of aroylhydrazones have been widely studied for several decades due to their structural and electronic properties and copious applications in various fields. Hydrazones exhibit amido–imidol tautomerism in solution, and various modes of coordination are found in their metal complexes.[8,9] The tautomeric forms of the ligands in their metal complexes are dependent on temperature, pH of the medium, nature of the substituents and the metal ions.[10] The possibility of tautomerism in this class of compounds has led to an interest in the field of pharmacology and catalysis.[11,12] Hydrazones and their metal complexes evince a variety of biological and pharmacological activities, such as anti-inflammatory,[13] anti-hypertensive,[14] anti-microbial,[15] anti-cancer,[16] anti-tuberculous[17] and antioxidant[18] activities.

The di-*tert*-butylphenols represent a potent class of anti-fungal, anti-oxidant[19] and well-known anti-inflammatory agents which are dual COX/LOX inhibitors.[6,20] Recently, Ghatak and co-workers have investigated the application of di-*tert*-butylphenylhydrazones as inhibitors of pro-inflammatory agents, such as COX-2 and 5-LOX enzymes.[21] A literature survey reveals that di-*tert*-butylphenolhydrazone derivatives could be considered as successful pharmacophores in the design of effective anti-inflammatory drugs with a superior safety profile. The coordination of bioactive organic molecules and anti-inflammatory drugs with metal ions is a common approach for enhancing the therapeutic potency and reducing the toxicity of the organic molecules.[22,23] Previous studies have shown that the metal complexes of anti-inflammatory drugs available on the market exhibited more potent anti-inflammatory activity than the drug itself in rats or mice, with fewer adverse effects.[24,25]

Encouraged by earlier reports, the work presented here focused on the synthesis, characterization, crystal structures, Hirshfeld surface analysis and anti-inflammatory activity of first row transition metal complexes derived from tridentate (*E*)-*N*′-(3,5-di-*tert*-butylsalicylidene)-2-(4-fluorobenzamido)benzohydrazide (LH_2). The potential binding interactions between the synthesized compounds and proteins (COX-2 and 5-LOX) were explored using molecular docking studies.

2 | EXPERIMENTAL PROTOCOLS

2.1 | Materials and Physical Measurements

The chemicals used were of analytical reagent grade and used without further purification. Hydrated metal salts were used as supplied. Carbon, hydrogen and nitrogen were determined using a Thermoquest CHN analyser. Metal contents of the complexes were determined according to a literature procedure.[26] Infrared (IR) spectra were recorded with a Nicolet-6700 FT-IR spectrometer in the 400–4000 cm^{-1} region using KBr discs. ^1H NMR (400 MHz) and ^{13}C NMR (100 MHz) spectra were recorded with Bruker spectrometer, in deuterated dimethylsulfoxide (DMSO-d_6) with tetramethylsilane as an internal standard. Mass spectra were recorded with a Waters XEVO TQS micro mass spectrometer and a Shimadzu QP 2010S GC mass spectrometer. Electron paramagnetic resonance (EPR) spectra of $[Cu(L)(H_2O)]$ were recorded at both room temperature and 77 K with a Varian E-4 X-band spectrometer using tetracyanoethylene as the g-marker. UV–visible spectra were recorded with a JASCO V-670 UV–visible spectrophotometer in the 200–1100 nm range using dimethylformamide (DMF) as the solvent. Conductance measurements of complexes (1 mM) were recorded in DMF using an ELICO-CM-82 conductivity bridge. Thermogravimetric (TG)/differential thermogravimetric analysis (DTA) studies of the metal complexes were carried out over the temperature range 25–1000 °C using a Universal V4.5A (TA Instruments).

2.2 | Synthesis of LH_2

A schematic of the synthesis of LH_2 is shown in Scheme 1. In the first step, 4-fluorobenzoyl chloride (1.51 g, 10 mmol) was added dropwise to a solution of methyl anthranilate (**I**; 1.58 g, 10 mmol) in benzene (200 ml) and stirred for 3 h at room temperature to afford methyl 2-(4-fluorobenzamido)benzoate (**II**; yield: 89%). In the second step, 99% hydrazine hydrate (5 g, 0.1 mol) was added to a methanolic solution of **II** (2.73 g, 10 mmol) and refluxed for 4 h to afford 2-(4-fluorobenzamido)benzohydrazide (**III**; yield: 74%). Finally, a methanolic solution of 3,5-di-

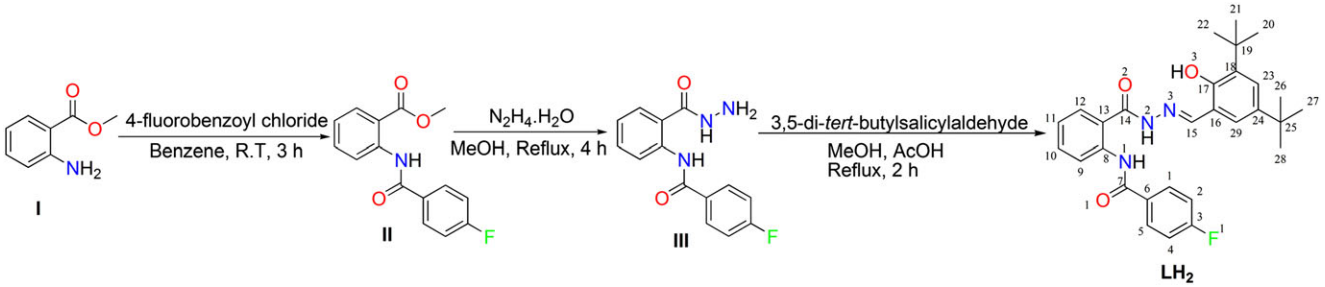

SCHEME 1 Synthetic route for preparation of LH_2

tert-butyl-2-hydroxybenzaldehyde (2.34 g, 10 mmol) was added to a methanolic suspension of **III** (2.73 g, 10 mmol). The reaction mixture along with a catalytic amount of glacial acetic acid (five drops) was continuously stirred and further refluxed for 2 h. Progress of the reaction was monitored by TLC. The resulting solid was filtered off, washed with cold methanol and dried in air.

LH_2. Colour: white; yield: 86%; m.p. 264–266 °C. Anal. Calcd for $C_{29}H_{32}FN_3O_3$ (%): C, 71.14; H, 6.59; N, 8.58. Found (%): C, 70.90; H, 6.40; N, 8.46. IR (KBr, cm^{-1}): 3443 (O—H, broad), 3319, 3215 (N1—H, N2—H), 1680 (C7=O1), 1634 (C14=O2), 1596 (C=N), 1279 (C—O). ^1H NMR (400 MHz, DMSO-d_6, δ, ppm): 1.25 (9H, s, *tert*-Bu), 1.38 (9H, s, *tert*-Bu), 7.12 (1H, d, C23H, J = 2 Hz), 7.31–7.28 (2H, m, C2H & C4H), 7.44–7.40 (2H, m, C11H & C29H), 7.63 (1H, t, C10, J = 8 Hz), 7.87 (1H, d, C9, J = 8 Hz), 8.01–7.98 (2H, m, C1H & C5H), 8.42 (1H, d, C12H, J = 8 Hz), 8.56 (1H, s, C15H), 11.65 (1H, s, O3H, D_2O exchange), 12.14 (1H, s, N2H, D_2O exchange), 12.38 (1H, s, N1H, D_2O exchange). ^{13}C NMR (100 MHz, DMSO-d_6, δ, ppm): 31.20 ($(CH_3)_3$), 33.82 ($(CH_3)_3$), 29.25 (C—$(CH_3)_3$), 34.58 (C—$(CH_3)_3$), 115.78 (C2,C4), 116 (C16), 121.59 (C29), 125.85 (C23), 129.73 (C1, C5), 130.93 (C6), 138.96, 116.79, 132.63, 123.38, 128.62, 120.78 (C8-13, aromatic), 135.68 (C18), 140.52 (C24), 152.33 (C15), 154.65 (C17), 163.67 (C14), 164.36 (C7). UV–visible: λ_{max} (DMF): 272, 300 nm.

2.3 | Synthesis of Metal Complexes

A schematic of the synthesis of the complexes is shown in Scheme 2.

2.3.1 | Synthesis of $[Co(L)(LH)]\cdot H_2O$

A mixture of LH_2 (0.490 g, 1.0 mmol) and $Co(CH_3COO)_2\cdot 4H_2O$ (0.124 g, 0.5 mmol) in 30 ml of methanol was refluxed for 6 h. The reddish brown precipitate obtained was filtered off, washed with cold methanol and dried in air. Single crystals suitable for X-ray diffraction studies were obtained by slow evaporation of the filtrate.

Colour: reddish brown; yield: 74%. Anal. Calcd for $C_{58}H_{63}CoF_2N_6O_7$ (%): C, 66.15; H, 6.03; Co, 5.60; N, 8.58. Found (%): C, 66.22; H, 5.91; Co, 5.52; N, 7.83. IR (KBr, cm^{-1}): 3433 (O—H, broad), 3367 (N1—H), 1680 (C7=O1), 1586 (C=N), 1615 (C=N, new), 1235 (C—O). ESI-MS (m/z): 1035 $[M - H_2O + H]^+$. UV–visible: λ_{max} (DMF): 271, 325, 439 nm. Molar conductance (Ω^{-1} cm^2 mol^{-1}): 3.43.

2.3.2 | Synthesis of [Ni(L)(DMF)]

A mixture of LH_2 (0.490 g, 1.0 mmol), sodium acetate (0.164 g, 2.0 mmol) and $NiCl_2\cdot 6H_2O$ (0.24 g, 1.0 mmol) in 30 ml of methanol was refluxed for 6 h. The reddish brown precipitate obtained was filtered, washed with hot methanol and dried in air. Further, the precipitate was dissolved in 30 ml of DMF. Single crystals suitable for X-ray diffraction studies were obtained by slow evaporation of the solution over a period of 10–11 days.

Colour: reddish brown; yield: 59%. Anal. Calcd for $C_{32}H_{37}FN_4NiO_4$ (%): C, 62.06; H, 6.02; Ni, 9.48; N, 9.05. Found (%): C, 61.97; H, 5.94; Ni, 9.35; N, 8.91. IR (KBr, cm^{-1}): 3446 (N1—H), 1671 (C7=O1), 1588 (C=N), 1621 (C=N, new), 1235 (C—O). ESI-MS (m/z): 619 $[M + H]^+$. UV–visible: λ_{max} (DMF): 272, 361, 420 nm. Molar conductance (Ω^{-1} cm^2 mol^{-1}): 7.55.

2.3.3 | Synthesis of $[Cu(L)(H_2O)]$

A mixture of LH_2 (0.490 g, 1.0 mmol) and $Cu(CH_3COO)_2\cdot H_2O$ (0.20 g, 1.0 mmol) in 30 ml of methanol was stirred for 3 h at room temperature. The resultant solution on slow evaporation afforded green crystals of $[Cu(L)(H_2O)]$, suitable for X-ray diffraction studies.

Colour: green; yield: 77%. Anal. Calcd for $C_{29}H_{32}CuFN_3O_4$ (%): C, 61.20; H, 5.67; Cu, 11.17; N, 7.38. Found (%): C, 61.15; H, 5.55; Cu, 11.03; N, 7.25. IR (KBr, cm^{-1}): 3439 (O—H, broad, N1—H), 1673 (C7=O1), 1584 (C=N), 1612 (C=N, new), 1238 (C—O). ESI-MS (m/z): 569 $[M + H]^+$. UV–visible: λ_{max} (DMF): 272, 323, 413, 635 nm. Molar conductance (Ω^{-1} cm^2 mol^{-1}): 6.32.

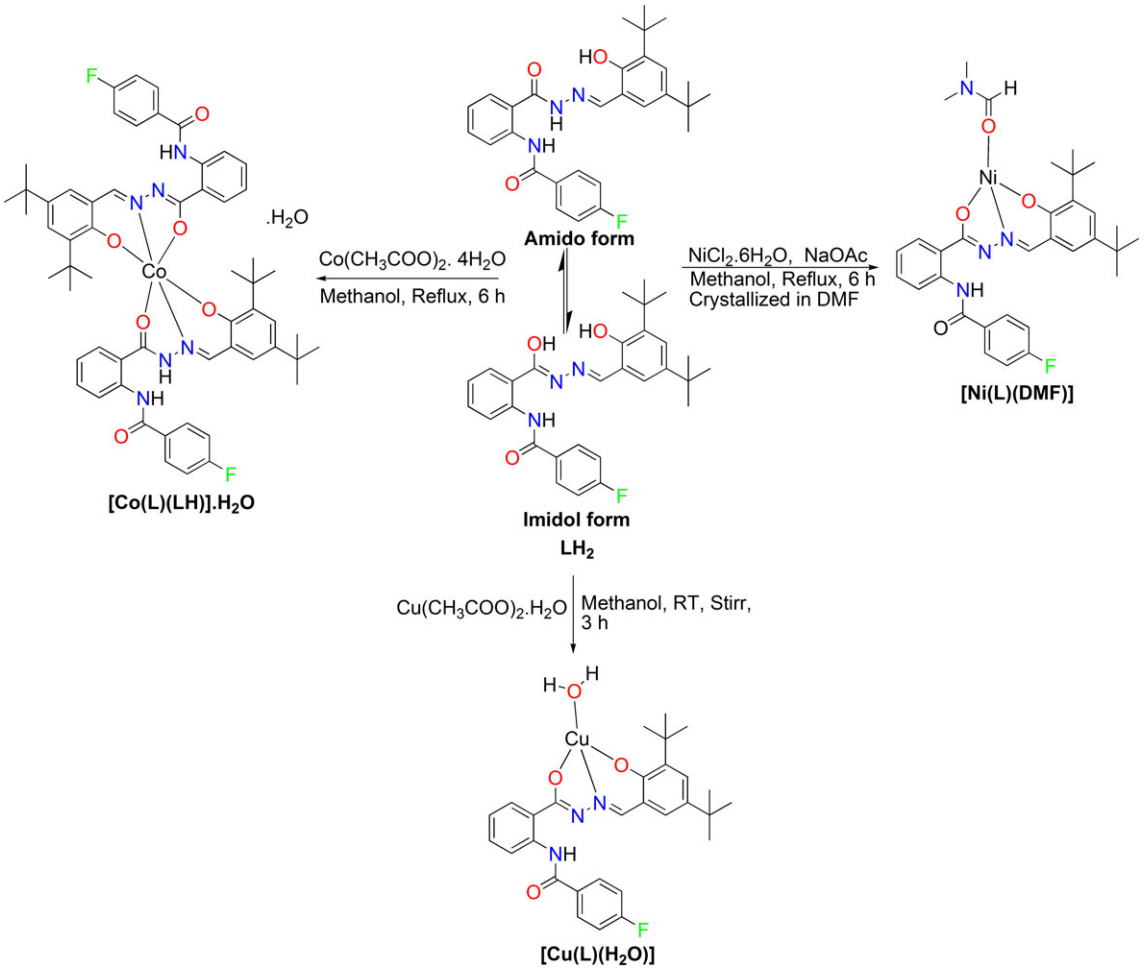

SCHEME 2 Synthetic route for preparation of complexes

2.4 | Single-Crystal X-ray Crystallographic Studies

Single-crystal X-ray data of all the complexes were collected at 100 K with a Rigaku SuperNova Dualflex AtlasS2 diffractometer using Cu Kα radiation (λ = 1.54184 Å). Integration, absorption correction and determination of unit cell parameters were performed using the CrysAlisPro program package.[27] The structures were solved by a direct method with SHELXD-2014/6 and refined against F^2 by the full-matrix least-squares technique in the anisotropic approximation (except hydrogen atoms) using the SHELXL-2014/6 package.[28] Hydrogen atom positions were calculated geometrically and refined using the riding model. Mercury CSD 2.0 program[29] was used for molecular graphics.

2.5 | Hirshfeld Surface (HS) Analysis

The molecular HSs were mapped with d_{norm}, and two-dimensional (2D) fingerprint plots were generated using Crystal Explorer 3.1[30] based on the pertinent CIF files. Three-dimensional HS maps generated with d_{norm} using a red, white and blue colour scheme give a precise picture of close contacts, van der Waals contacts and longer contacts.[31] The combination of d_e (distance from any surface point to the nearest exterior atom) and d_i (distance from any surface point to the nearest interior atom) in the form of a 2D fingerprint plot provides summary of intermolecular contacts in the crystal.[32,33]

2.6 | Molecular Docking Simulation

High-resolution crystallographic structures of celecoxib-bound COX-2 (PDB ID: 3LN1) and human 5-LOX (PDB ID: 3O8Y) were retrieved from the RSC Protein Data Bank. AutoDock Tools and AutoDock Vina[34] were employed to set up and perform docking calculations of LH_2 and its complexes in their binding to proteins. The metal complexes were taken from their crystal structures as a CIF file and were converted to the PDB format using Mercury software. The geometrical optimization of LH_2

was done using density functional theory with the ORCA computational chemistry package.[35] All calculations were performed using the hybrid functional BP in combination with the Ahlrichs split-valence double-ξ basis set def2-SVP[36] for all the atoms. The output of the calculations was visualized using the molecular visualizer tool Avogadro 1.1.1.[37]

In docking analysis, the binding site was assigned to include the entire protein, which was enclosed in a grid box with dimensions 60 × 60 × 60 Å^3 and a grid spacing of 0.765 Å. The genetic algorithm population size and the maximum number of evaluations were 150 and 2 500 000, respectively. A total of 50 runs were carried out. A maximum of 50 conformers were considered for each molecule and the root-mean-square cluster tolerance was set to 2.0 Å in each run. Discovery Studio 4.1.0 and Python Molecule Viewer[38] were used to explore the results obtained.

2.7 | Anti-inflammatory Screening

Male Sprague Dawley rats (H. S. K. College of Pharmacy, Bagalkot, India) weighing 160–220 g housed at 25 ± 2 °C were fasted with free access to water at least 16–22 h prior to experiments. A paw oedema was induced by injecting 1% λ-carrageenan (0.2 ml in 0.9% NaCl) subcutaneously in the sub-plantar region of right hind paw. Animals were divided into groups of six each. The rat paw thickness was measured with a digital plethysmometer (UGO Basile 7140) before and 1 h after carrageenan injection to detect the carrageenan-induced inflammation. The test compounds were suspended in 0.5% sodium carboxymethylcellulose (Na-CMC) and administered at doses of 5 and 10 mg kg^{-1} of body weight and diclofenac was administered orally at a dose of 10 mg kg^{-1} to all groups of rats 1 h after carrageenan injection. The control groups received 0.5% Na-CMC in distilled water. Changes in paw volume, in millilitres, were recorded at 0.5, 1, 3 and 5 h after injection of the test compounds, reference drug and control. For statistical analysis, we used GraphPad Prism 3.0. Results were expressed in terms of oedema volume as mean ± SEM and mean percent inhibition. The oedema inhibition was calculated according to the following equation:

$$\text{Oedema inhibition } (\%) = \frac{V_c - V_t}{V_c} \times 100$$

where V_c is the oedema volume of rat of control group, at time t, and V_t is the oedema volume of rat of test compound group, at time t.

3 | RESULTS AND DISCUSSION

LH_2 and its complexes are soluble in chloroform, DMF and DMSO. Analytical data for all the compounds are in good agreement with their proposed formulae. Analytical, physicochemical and spectral parameters are compiled in Section 2.

3.1 | IR Spectral Data

The numbering scheme followed for LH_2 is given in Scheme 1. The *tert*-butyl substituent groups in LH_2 and its complexes are conspicuous by their typical absorption patterns between 2870 and 2955 cm^{-1}.[39] The IR spectrum of LH_2 (Figure S1) shows a broad band at 3443 cm^{-1} attributed to free ν(O—H). Absence of this band in the spectra of all the complexes indicates deprotonation of the phenolic oxygen and subsequent coordination to the metal. In addition, the ν(C—O) band observed at 1279 cm^{-1} in the spectrum of LH_2 shows a blue shift by 30–40 cm^{-1} suggesting the coordination of phenolic oxygen to the metal ion. The ν(C=N) band appearing at 1596 cm^{-1} in the LH_2 spectrum is shifted towards lower frequency upon complexation, indicating the involvement of azomethine nitrogen in coordination.

The sharp bands at 1680 and 1634 cm^{-1} in the LH_2 spectrum are assigned to ν(C7=O1) and ν(C14=O2), respectively.[40] The band due to ν(C7=O1) remains almost unaltered in the spectra of all the complexes suggesting its non-involvement in coordination. The absence of bands due to ν(C14=O2) and ν(N2—H) (3215 cm^{-1}) and the appearance of a new band in the region 1610–1620 cm^{-1} due to the stretching vibration of the conjugated —C=N—N=C— moiety in the complexes[41] indicate the enolization and subsequent coordination of oxygen atom to the central metal ion. In addition, the ν(C14=O2) band at 1634 cm^{-1} undergoes a substantial red shift to 1624 cm^{-1} in the spectrum of [Co(L)(LH)]·H_2O (Figure S2) indicating the presence of both imidol (L^{2-}) and amido (LH^-) tautomers of the ligand in the complex. The strong absorption band at 1639 cm^{-1} in the spectrum of [Ni(L)(DMF)] (Figure S3) is attributed to the characteristic stretching mode of >C=O present in the coordinated DMF molecule.[42] A medium intensity band at 3319 cm^{-1} is assigned to ν (N1H) of LH_2. This band is not observed for the complexes and might be obscured by the broad band in the region 3433–3446 cm^{-1}, due to the water molecules present in the complexes.

3.2 | ^{1}H NMR and ^{13}C NMR Studies

The ^{1}H NMR spectrum of LH_2 was recorded in the range 0–20 ppm and is presented in Figure S4. The signals at 12.38, 12.14 and 11.65 ppm are attributed to the D_2O-exchangeable N2H, N1H and O3H protons, respectively. The two singlets at 1.25 and 1.38 ppm correspond to two sets of magnetically non-equivalent *tert*-butyl groups.[43] The singlet at 8.56 ppm is assigned to the azomethine proton (C15H), which confirms the formation of hydrazone. The aromatic protons resonate in the range 7.12–8.42 ppm. The D_2O exchange ^{1}H NMR spectrum of LH_2 is provided in the supporting information (Figure S5).

The ^{13}C NMR spectrum of LH_2 (Figure S6) shows signals at 164.36 and 163.67 ppm and are assigned to the carbonyl (C7 and C14) carbons, respectively. A singlet at 152.32 ppm ascribed to the azomethine carbon (C15) confirms the formation of hydrazone functionality. The two intense bands observed at 31.20 and 33.82 ppm correspond to methyl carbons (—$(CH_3)_3$) of two non-equivalent *tert*-butyl groups.

3.3 | Mass Spectral Studies

The ESI mass spectrum of LH_2 (Figure S7) shows a molecular ion $[M]^+$ peak at 489. That of $[Co(L)(LH)]\cdot H_2O$ (Figure S8) shows a molecular ion $[M - H_2O + H]^+$ peak at 1035. This assignment is in good agreement with the ascribed +3 oxidation state for cobalt. ESI mass spectral studies of [Ni(L)(DMF)] and $[Cu(L)(H_2O)]$ (Figure S9) show their molecular ion $[M + H]^+$ peaks at 619 and 569, respectively. Apart from this, spectra show additional peaks, which are due to molecular cations of various fragments of the complexes and isotopes.

3.4 | Electronic and EPR Spectral Studies

Electronic spectra of LH_2 and its complexes (Figure S10) were measured in DMF. The free ligand exhibits strong absorptions at 272 and 300 nm. The former is assigned to $\pi \rightarrow \pi^*$ transition while the latter to $n \rightarrow \pi^*$ transition.[44] The band at 272 nm remains unchanged in the spectra of the complexes. The absorption at 300 nm undergoes a red shift upon complexation. This indicates the donation of a lone pair of electrons to the metal ion and hence the involvement of azomethine nitrogen in coordination. No d–d transitions could be observed in the case of $[Co(L)(LH)]\cdot H_2O$ and [Ni(L)(DMF)]. Absence of any electronic transition at longer wavelength indicates a large crystal-field splitting. A broad band in the electronic spectrum of $[Cu(L)(H_2O)]$ with peak maximum at 635 nm is assigned to the combination of $^2B_{1g} \rightarrow {}^2A_{1g}$ and $^2B_{1g} \rightarrow {}^2E_g$ transitions as for a square planar configuration around the metal ion.[45] All the complexes show an intense band at 410–440 nm, which can be assigned to charge transfer transitions.

X-band EPR measurements were carried out in powder form as well as in frozen solution of $[Cu(L)(H_2O)]$ in DMSO. The EPR spectrum of powder sample exhibits isotropic intense broad signal with $g_{iso} = 2.04$ with no hyperfine splitting. From solution EPR measurements, it was possible to resolve the hyperfine pattern (Figure S11) with $g_{\parallel} = 2.30$, $g_{\perp} = 2.05$, $G = 6.51$, $A_{\parallel} = 182 \times 10^{-4}$ cm^{-1} and $A_{\perp} = 57 \times 10^{-4}$ cm^{-1}. From the observed g values, $g_{\parallel} > g_{\perp} > g_e$ (2.0023), it is evident that the unpaired electron is localized in $d_{x^2-y^2}$ orbital of the Cu(II) ion and the spectrum is characteristic of axial symmetry.[46] The quotient $g_{\parallel}/A_{\parallel}$ measures the degree of tetrahedral distortion. This quotient ranges from approximately 105 to 135 cm for square planar structures. The $g_{\parallel}/A_{\parallel}$ value of 126 cm for $[Cu(L)(H_2O)]$ is in agreement with the crystallographic data.[47] Further, it is expected that there is no exchange coupling between two copper centres in the solid state, as the axial symmetry parameter $G = g_{\parallel} - 2/g_{\perp} - 2$ is found to be more than 4 for the complexes.[48]

3.5 | Thermal Analysis

Thermal behaviour of all the complexes was studied over the temperature range 25–1000 °C under nitrogen atmosphere. TG/DTA curves of $[Co(L)(LH)]\cdot H_2O$ (Figure S12) show the first exothermic weight loss (1.96%, calcd 1.71%) at 150 °C which is consistent with the removal of hydrogen-bonded lattice-held water molecule. In the second stage, part of the ligand is lost in the range 230–330 °C with an exothermic DTA curve at 270 °C. Further mass loss (43%) in the range 330–430 °C is ascribed to the decomposition of the remaining part of the ligand. The plateau obtained above 430 °C corresponds to the formation of stable metal oxide with residual weight of 7.8%. The first weight loss of 12.02% (calcd 11.80%) between 230 and 330 °C exhibited by [Ni(L)(DMF)] (Figure S13) is accounted for by the loss of a coordinated DMF molecule. The second weight loss of 75.7% between 220 and 410 °C corresponds to the loss of one ligand molecule. The corresponding DTA peak at 400 °C for the complex signifies the exothermic process. The plateau obtained above 410 °C corresponds to the formation of stable NiO. $[Cu(L)(H_2O)]$ shows an initial weight loss of 3.32% (calcd 3.16%) between 130 and 150 °C and can be accounted for by the loss of a coordinated water molecule. The dehydrated complex then decomposes in a single

step, leaving behind stable CuO above 460 °C with a residue of 12.2%.

3.6 | Molecular Structures of [Co(L)(LH)]·H_2O, [Ni(L)(DMF)] and [Cu(L)(H_2O)]

The solid-state structures of all the complexes were analysed using single-crystal X-ray studies. Details of the crystallographic data collection and the parameters of the refinement process are summarized in Table 1. Perspective ORTEP views of [Co(L)(LH)]·H_2O, [Ni(L)(DMF)] and [Cu(L)(H_2O)] along with the atom numbering schemes are depicted in Figures 1–3, respectively. A summary of the bond lengths and bond angles is given in Table 2. Relevant hydrogen bond interactions are compiled in Table 3.

The asymmetric unit of [Co(L)(LH)]·H_2O contains a neutral [Co(L)(LH)] and one lattice-held water of crystallization. The two inequivalent ONO tridentate ligands

TABLE 1 Crystal data and structure refinement details of complexes [Co(L)(LH)]·H_2O, [Ni(L)(DMF)] and [Cu(L)(H_2O)]

	[Co(L)(LH)]·H_2O	[Ni(L)(DMF)]	[Cu(L)(H_2O)]
Empirical formula	$C_{58}H_{63}CoF_2N_6O_7$	$C_{32}H_{37}FN_4NiO_4$	$C_{29}H_{32}CuFN_3O_4$
Formula weight	1053.07	619.36	569.11
Temperature (K)	100 (1)	100 (1)	100 (1)
Wavelength (Å)	1.54184	1.54184	1.54184
Crystal system	Monoclinic	Monoclinic	Monoclinic
Space group	$P2_1/n$	$P2_1/n$	$P2_1/n$
Unit cell dimensions			
a (Å)	16.1762 (7)	13.58381 (15)	14.1773 (3)
b (Å)	23.4349 (9)	9.45350 (10)	9.43391 (18)
c (Å)	14.7596 (6)	23.9224 (2)	21.2097 (4)
α (°)	90	90	90
β (°)	98.447 (4)	92.6059 (9)	104.267 (2)
γ (°)	90	90	90
Volume (Å^3)	5534.5 (4)	3068.81 (6)	2749.25 (9)
Z	4	4	4
Density (calculated) (g cm^{-3})	1.264	1.341	1.375
Absorption coefficient (mm^{-1})	2.950	1.312	1.503
F(000)	2216.0	1304.0	1188.0
Crystal size (mm^3)	0.249 × 0.125 × 0.107	0.426 × 0.408 × 0.207	0.136 × 0.115 × 0.056
2θ range for data collection (°)	5.522 to 148.986	7.344 to 148.978	6.8 to 148.982
Index ranges	$-20 \le h \le 13$, $-27 \le k \le 29$, $-17 \le l \le 18$	$-16 \le h \le 16$, $-11 \le k \le 11$, $-29 \le l \le 23$	$-17 \le h \le 17$, $-8 \le k \le 11$, $-26 \le l \le 19$
Reflections collected	25 876	14 274	12 172
Independent reflections	11 321 [R_{int} = 0.0286, R_{sigma} = 0.0366]	6250 [R_{int} = 0.0140, R_{sigma} = 0.0167]	5623 [R_{int} = 0.0169, R_{sigma} = 0.0230]
Completeness	99.9% (to θ = 74.493°)	99.9% (to θ = 74.489°)	100% (to θ = 74.491°)
Absorption correction	Gaussian	Gaussian	Multi-scan
Data/restraints/parameters	11321/0/699	6250/0/391	5623/0/361
Goodness-of-fit on F^2	1.020	1.014	1.001
Final R indexes [$I \ge 2\sigma(I)$]	R_1 = 0.0414, wR_2 = 0.0995	R_1 = 0.0309, wR_2 = 0.0836	R_1 = 0.0308, wR_2 = 0.0822
Final R indexes [all data]	R_1 = 0.0555, wR_2 = 0.1072	R_1 = 0.0323, wR_2 = 0.0846	R_1 = 0.0367, wR_2 = 0.0856
Largest diff. peak and hole/e Å^{-3}	0.33/−0.40	0.27/−0.43	0.31/−0.45

(differing in their protonation state, Scheme 2) are coordinated to Co(III) in an octahedral field preserving electroneutrality of the molecule as a whole. In the coordination sphere, both the ligands (L^{2-} and LH^{-}) are almost perpendicular to each other. The mean planes of the two ligands have a dihedral angle of 84.08°. Azomethine nitrogens (N3 and N6) of the two ligands reside *trans* to each other whereas the other two donor sites ((O2, O5) and (O3, O6)) remain *cis* to each other. The imino nitrogen atoms are axially positioned (Co1—N3 1.877(15) Å and Co1—N6 1.855(15) Å) and four oxygen atoms constitute the equatorial plane of the octahedron. The bite angles for the ligands (L^{2-} and LH^{-}) lie in the range 82.84–94.20°, indicating a distortion from an ideal octahedral geometry,[49] with the *trans*-donor bond angles in the range 174.9(3)–177.7(3)° and the *cis*-donor bond angles in the range 87.0(3)–94.7(3)°. The Co1—$O_{phenolate}$ bond distances of 1.864(13) and 1.857(13) Å are for Co1—O3 and Co1—O6 bonds, respectively. The Co1—$O2_{amido}$ and Co1—$O5_{imidol}$ bond distances are 1.957(13) and 1.930(13) Å, respectively. By comparing the bond distances, the O5 atom of the doubly deprotonated ligand (L^{2-}) is found to be more strongly bound to the Co(III) ion than the O2 atom of the singly deprotonated ligand (LH^{-}). The coexistence of both the tautomeric forms of ligand within a complex is substantiated by the bond distances in the region of five-membered chelate rings. The C14—$O2_{amido}$ (1.267(2) Å) and C43—$O5_{imidol}$ (1.309(2) Å) differ in their lengths. The N2—C14 (1.326(2) Å) is more of σ in character compared to N5—C43 (1.306(2) Å). $[Co(L)(LH)]\cdot H_2O$ is stabilized by a number of intramolecular

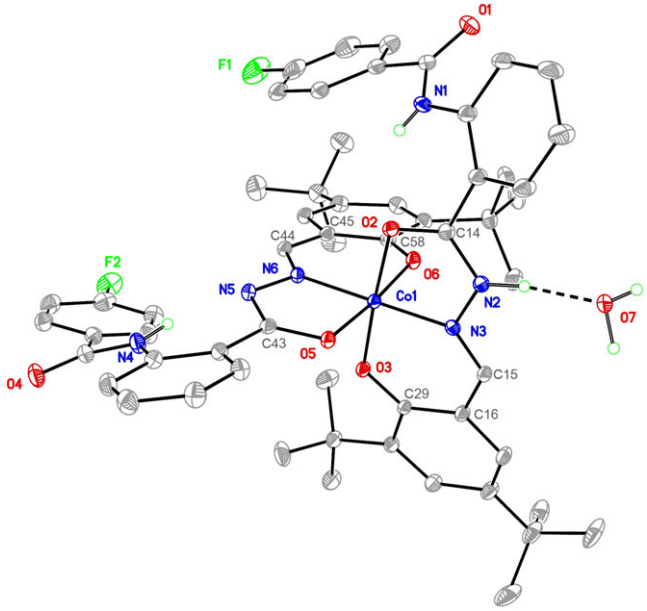

FIGURE 1 ORTEP projection (drawn at 30% probability level) of $[Co(L)(LH)]\cdot H_2O$ with partial atom labelling scheme

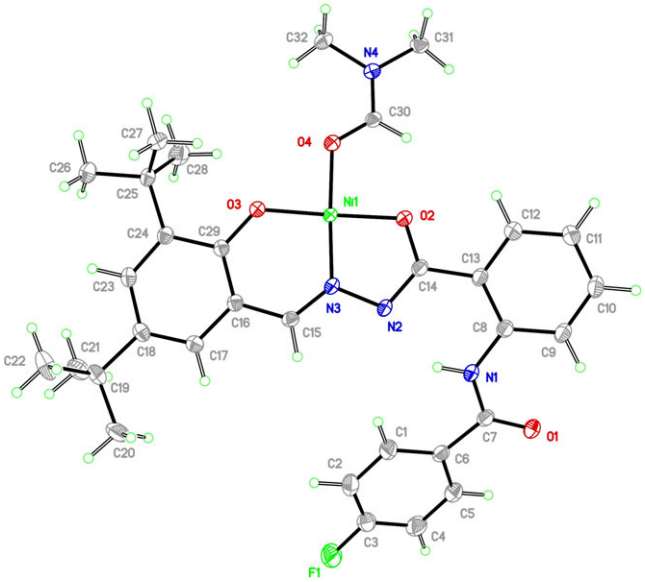

FIGURE 2 ORTEP projection of [Ni(L)(DMF)] showing 50% probability ellipsoids

N2—H2···O7(W) (2.63(2) Å), N1—H1···O2 (2.73(2) Å) and N4—H4···N5 (2.63(2) Å) and intermolecular O7(W)—H7A···O4 (2.721(2) Å) and O7(W)—H7B···O5 (2.77(2) Å) hydrogen bonds (Figure S14). Lattice-held water molecule is involved in three different hydrogen interactions. O7 of lattice water acts as donor to the carbonyl oxygens O4 and O5 of two adjacent molecules and also as an acceptor to amide nitrogen N2. In addition, the complex exhibits C—H···π and Cg···Cg interactions. Intramolecular C—H···π interactions are observed between *tert*-butyl hydrogens (H56A, H27A) and six-membered chelate rings ((Co1/O3/C29/C16/C15/N3), (Co1/O6/C58/C45/C44/N6)), respectively. An intermolecular stacking occurs between the centroids of two phenyl rings ((C45/C46/

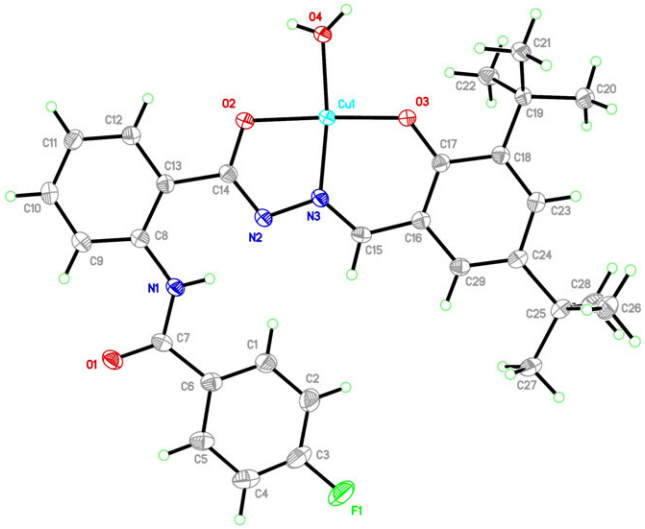

FIGURE 3 ORTEP projection of $[Cu(L)(H_2O)]$ showing 50% probability ellipsoids

TABLE 2 Selected bond lengths and angles of complexes [Co(L)(LH)]·H_2O, [Ni(L)(DMF)] and [Cu(L)(H_2O)]

[Co(L)(LH)]·H_2O					
Bond lengths (Å)					
Co1–N6	1.855(15)	Co1–O2	1.957 (13)	N2–C14	1.326 (2)
Co1–O6	1.857(13)	O2–C14	1.267 (2)	N3–C15	1.290 (2)
Co1–O3	1.864(13)	O3–C29	1.314 (2)	N5–C43	1.306 (2)
Co1–N3	1.877(15)	O5–C43	1.309 (2)	N6–C44	1.292 (2)
Co1–O5	1.930(13)	O6–C58	1.320 (2)		
Bond angles (°)					
N6–Co1–O6	94.20 (6)	O6–Co1–O5	174.99 (6)	O3–Co1–O2	176.45 (5)
N6–Co1–O3	88.57 (6)	O3–Co1–O5	91.53 (6)	N3–Co1–O2	82.84 (6)
N6–Co1–N3	176.56 (7)	N3–Co1–O5	94.13 (6)	O5–Co1–O2	88.02 (5)
O6–Co1–N3	88.30 (6)	N6–Co1–O2	94.87 (6)	N6–Co1–O6	94.20 (6)
O3–Co1–N3	93.69 (6)	O6–Co1–O2	87.94 (6)	N6–Co1–O3	88.57 (6)
N6–Co1–O5	83.20 (6)				
[Ni(L)(DMF)]					
Bond lengths (Å)					
Ni1–N3	1.805 (10)	Ni1–O4	1.895 (9)	N3–C15	1.300 (16)
Ni1–O3	1.809 (8)	O2–C14	1.303 (15)	O3–C29	1.314 (15)
Ni1–O2	1.832 (9)	N2–N3	1.406 (13)	O4–C30	1.259 (15)
Bond angles (°)					
N3–Ni1–O3	95.99 (4)	O3–Ni1–O2	175.60 (4)	O3–Ni1–O4	86.86 (4)
N3–Ni1–O2	84.61 (4)	N3–Ni1–O4	175.57 (4)	O2–Ni1–O4	92.81 (4)
[Cu(L)(H_2O)]					
Bond lengths (Å)					
Cu1–O3	1.869 (11)	Cu1–O4	1.960 (12)	N2–C14	1.322 (2)
Cu1–N3	1.897 (13)	O2–C14	1.292 (19)	N2–N3	1.394 (17)
Cu1–O2	1.9191 (11)	O3–C17	1.317 (19)	N3–C15	1.291 (2)
Bond angles (°)					
O3–Cu1–N3	94.61 (5)	N3–Cu1–O2	82.36 (5)	N3–Cu1–O4	171.78 (6)
O3–Cu1–O2	176.70 (5)	O3–Cu1–O4	93.49 (5)	O2–Cu1–O4	89.57 (5)

C47/C52/C53/C58) and (C1—C6)) with a *Cg*···*Cg* distance of 3.832 Å (Figure S15).

[Ni(L)(DMF)] and [Cu(L)(H_2O)] have a distorted square planar geometry around the Ni(II) and Cu(II) ions in which the base plane is occupied by two oxygen atoms and one nitrogen atom of the doubly deprotonated *ONO* tridentate hydrazone (L^{2-}), while the fourth position is occupied by the oxygen atom (O4) of coordinated DMF and water molecule in [Ni(L)(DMF)] and [Cu(L)(H_2O)], respectively. The square planar geometry around Ni1 and Cu1 suffers some distortion which is evident from the chelate bite angles made by the ONO donor set of the ligand in both the complexes. The N3—Ni1—O2 and N3—Cu1—O2 angles (84.61° in [Ni(L)(DMF)] and 82.36° in [Cu(L)(H_2O)]) undergo compression whereas the N3—Ni1—O3 and N3—Cu1—O3 angles (95.99° in [Ni(L)(DMF)] and 94.61° in [Cu(L)(H_2O)]) undergo expansion from their ideal 90° value,[50] and this behaviour is anticipated because the compressed and expanded bite angles are enclosed by five-membered and six-membered chelate rings, respectively.

The molecular structure of [Ni(L)(DMF)] is stabilized by an intramolecular hydrogen bonding N1—H1A···N2 (2.71(14) Å) (Figure S16). [Cu(L)(H_2O)] is stabilized by strong intramolecular hydrogen bond N1—H1B···N2 (2.63(18) Å). In an extended crystal structure, an intermolecular hydrogen bond

TABLE 3 Hydrogen bond distances and bond angles in complexes [Co(L)(LH)]·H_2O, [Ni(L)(DMF)] and [Cu(L)(H_2O)]

D—H···A	*d*(D—H) (Å)	*d*(H—A) (Å)	*d*(D—A) (Å)	D—H—A (°)
[Co(L)(LH)]·H_2O				
N1—H1···O2	0.74 (2)	2.15 (2)	2.736 (2)	137 (2)
N2—H2···O7	0.91 (3)	1.73 (3)	2.632 (2)	171 (2)
N4—H4···N5	0.86 (3)	1.88 (3)	2.633 (2)	145 (2)
O7—H7A···O4#1	0.75 (3)	1.98 (3)	2.721 (2)	170 (3)
O7—H7B···O5#2	0.94 (3)	1.85 (3)	2.777 (2)	167 (3)
[Ni(L)(DMF)]				
N1—H1A···N2	0.841 (18)	2.015 (18)	2.7158 (14)	140.3 (16)
[Cu(L)(H_2O)]				
O4—H4C···O1#3	0.85 (3)	1.74 (3)	2.5829 (16)	177 (3)
N1—H1B···N2	0.84 (2)	1.90 (2)	2.6355 (18)	146 (2)

Symmetry codes: #1: $+X, +Y, -1+Z$; #2: $1-X, 1-Y, 1-Z$; #3: $\frac{1}{2}+X, \frac{3}{2}-Y, \frac{1}{2}+Z$.

O4—H4C···O1 is formed by O4 of the coordinated water molecule as a hydrogen bond donor towards the carbonyl oxygen atom O1 (2.58(16) Å) (Figure S17). In addition, [Cu(L)(H_2O)] is also stabilized by intermolecular *Cg*···*Cg* interaction between centroid of five-membered chelate ring (Cu1/O2/C14/N2/N3) and centroid of phenyl ring (C1—C6) with a *Cg*···*Cg* distance of 3.609 Å (Figure S18).

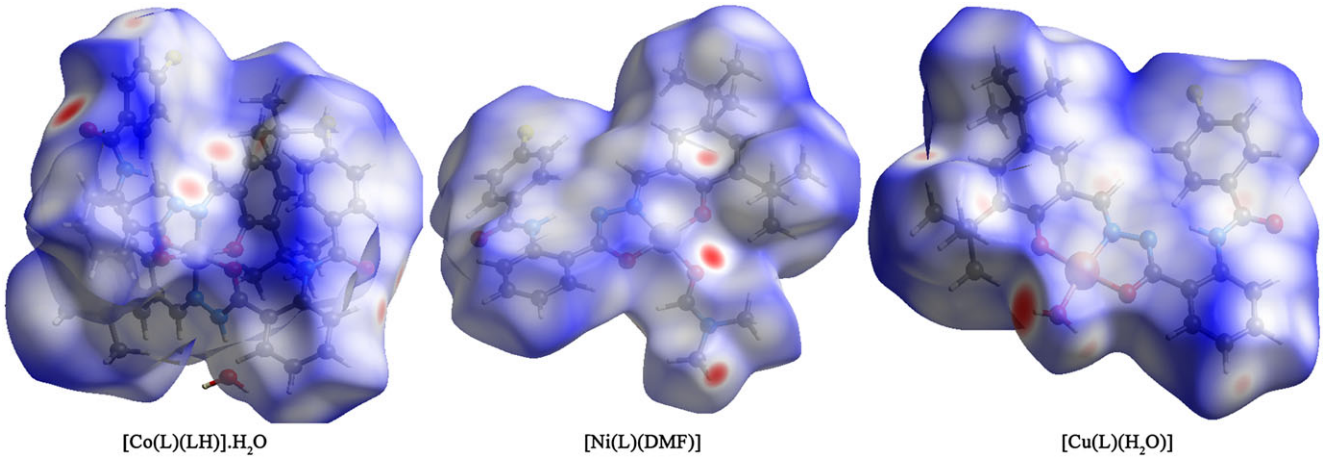

FIGURE 4 Hirshfeld surfaces mapped with d_{norm} of [Co(L)(LH)]·H_2O, [Ni(L)(DMF)] and [Cu(L)(H_2O)]

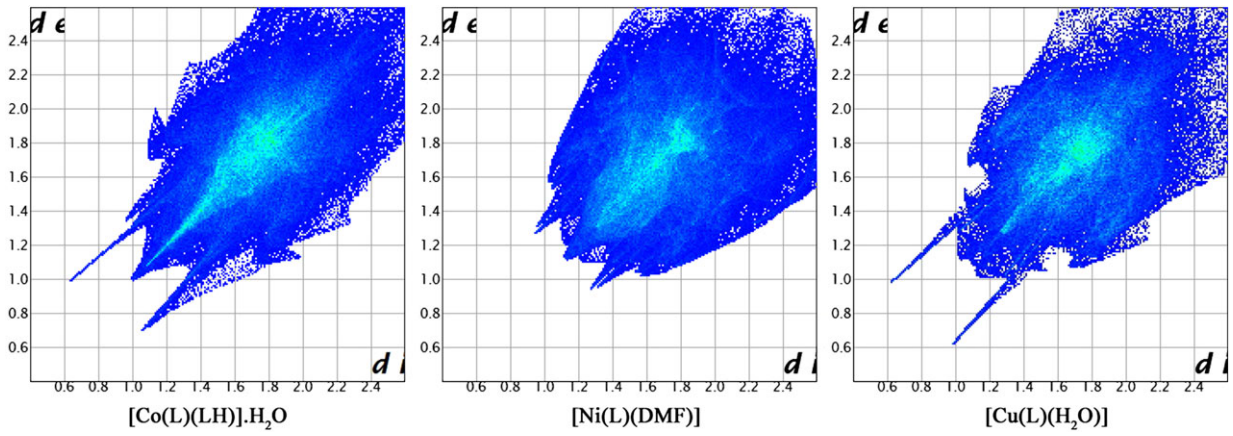

FIGURE 5 2D fingerprint plots of [Co(L)(LH)]·H_2O, [Ni(L)(DMF)] and [Cu(L)(H_2O)] showing all intermolecular interactions

TABLE 4 Relative contributions of various intermolecular interactions to the Hirshfeld surface area of complexes $[Co(L)(LH)]\cdot H_2O$, [Ni(L)(DMF)] and $[Cu(L)(H_2O)]$

Interaction	H···H (%)	C···H/H···C (%)	N···H/H···N (%)	O···H/H···O (%)	F···H/H···F (%)	C···C (%)	Other (%)
$[Co(L)(LH)]\cdot H_2O$	59.6	14.2	2.5	7.7	7.7	3.1	2.1
[Ni(L)(DMF)]	53.3	18.0	3.5	9.3	6.8	3.4	4.4
$[Cu(L)(H_2O)]$	50.9	18.8	3.4	6.4	7.9	2.6	8.4

3.7 | Hirshfeld Surface Analysis

HS analysis is a powerful technique for understanding the nature of intermolecular interactions within a crystal structure using a fingerprint plot.[51] HSs of the metal complexes are illustrated in Figure 4 showing surfaces mapped with d_{norm}. The information regarding intermolecular interactions which are summarized in Table 3 is visible by the spots on the Hirshfeld surfaces. The dominant O···H interactions are highlighted by the deep red area of d_{norm} surface. Light red spots are due to N—H···O and O—H···O interactions. Other visible spots in the surfaces are due to H···H contacts.[52] The H···H, O···H/H···O, C···H/H···C and N···H/H···N intermolecular interactions appear as distinct spikes in the 2D fingerprint plot (Figure 5). The proportion of O···H/H···O interactions comprise 7.7, 9.3 and 6.4% of the total HS area for each molecule of $[Co(L)(LH)]\cdot H_2O$, [Ni(L)(DMF)] and $[Cu(L)(H_2O)]$, respectively. In all the complexes, the spikes in the bottom left (donor) and bottom right (acceptor) area of the fingerprint plots represent the O···H and H···O interactions, respectively. The 'wings' seen in the fingerprint plot of $[Co(L)(LH)]\cdot H_2O$ belong to signature C—H···π interactions, with the 'wings' in the lower right and lower left of the fingerprint plot representing C—H···π acceptor and C—H···π donor interactions, respectively. The proportion of C···H/H···C interactions comprise 14.2, 18 and 18.8% of the total HS area for each molecule of $[Co(L)(LH)]\cdot H_2O$, [Ni(L)(DMF)] and $[Cu(L)(H_2O)]$, respectively. The C···H interactions in all the complexes are mainly due to neighbouring *tert*-butyl groups

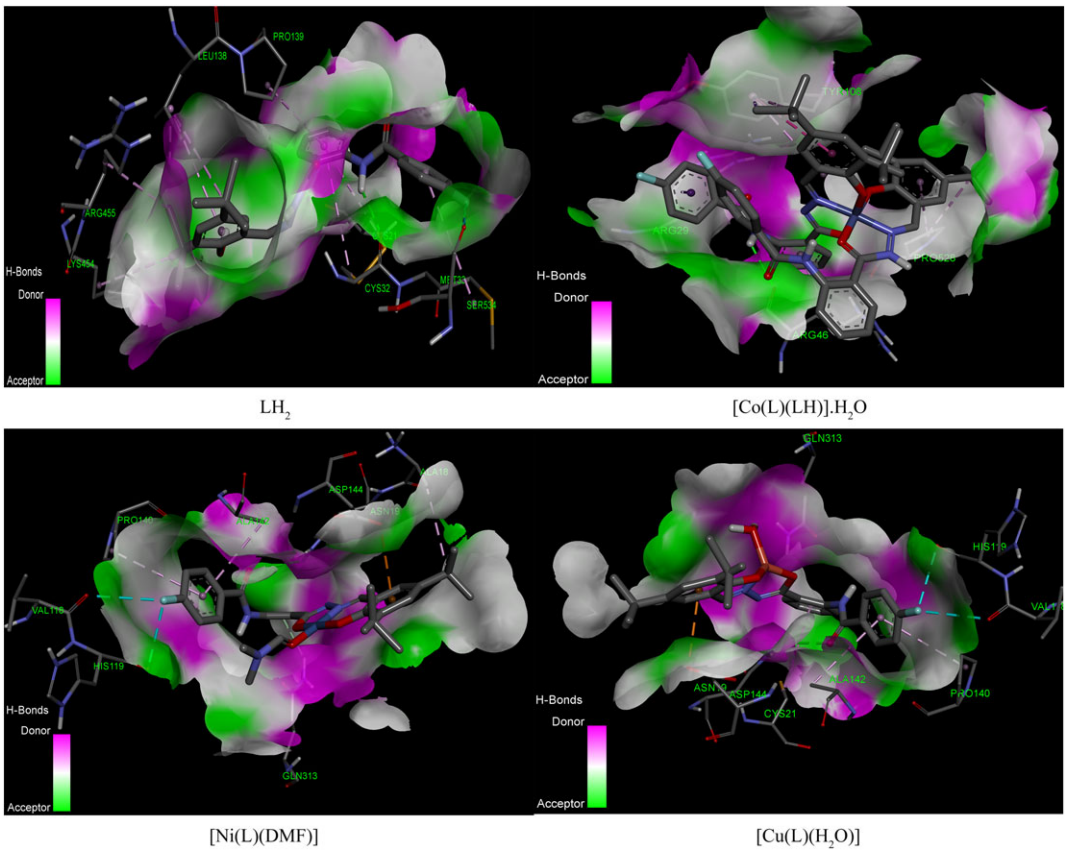

FIGURE 6 Docking figures of LH_2 and its metal complexes in COX-2 protein cavity

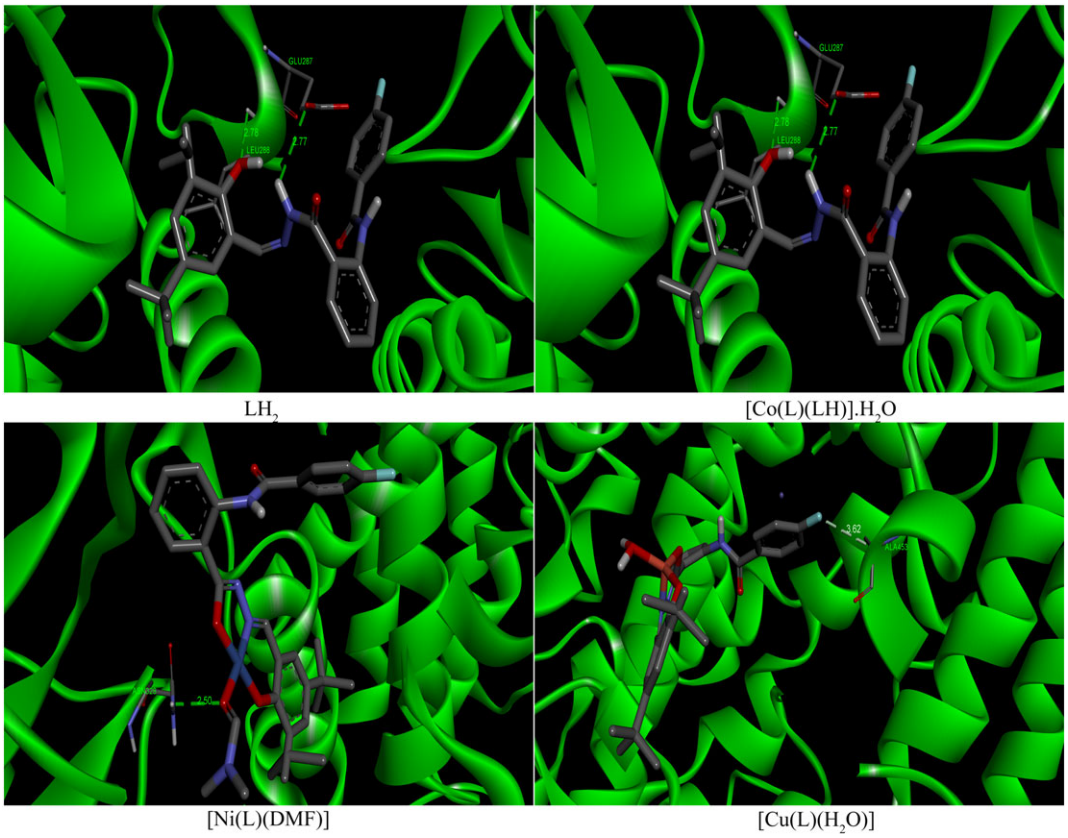

FIGURE 7 Docking figures of LH_2 and its metal complexes in 5-LOX protein cavity

pointing towards the aromatic ring of the phenol moiety. No significant C—H···π acceptor or donor interactions are observed for [Ni(L)(DMF)] and [Cu(L)(H_2O)]. The majority of contacts present in all the three complexes are due to H···H interactions. These interactions make up 50.9 to 59.6% of the Hirshfeld surface of the molecules. These contacts are mainly due to the *tert*-butyl groups present in the complexes.[53] The relative contributions of various intermolecular interactions to the Hirshfeld surface area are summarized in Table 4.

3.8 | Molecular Docking Studies

Molecular docking studies were performed to investigate interactions between the synthesized compounds and pro-inflammatory targets COX-2 and 5-LOX enzymes. These are the key enzymes involved in regulating the AA metabolic pathway and the production of pro-inflammatory prostaglandins and leukotrienes. Therefore, they have been validated as selective targets of anti-inflammatory drugs. LH_2 and its Co(III), Ni(II)

TABLE 5 Molecular docking results of LH_2 and its complexes in COX-2 and 5-LOX protein cavities

	COX-2				5-LOX			
Molecule	Binding energy (kcal mol^{-1})	No. of hydrogen bonds	Interacting residues	Distance (Å)	Binding energy (kcal mol^{-1})	No. of hydrogen bonds	Interacting residues	Distance (Å)
LH_2	−10.1	1	Cys32	2.24	−9.3	2	Glu287 Leu288	2.77 2.78
[Co(L)(LH)]·H_2O	−12.6	1	Arg46	2.54	−10.8	5	Arg246 Glu287	2.21, 2.21 1.84, 2.45 2.83
[Ni(L)(DMF)]	−10.5	1	Asn19	2.98	−9.6	1	Asn328	2.50
[Cu(L)(H_2O)]	−11.8	1	Asn19	2.8	−9.4	1	Ala453	3.62

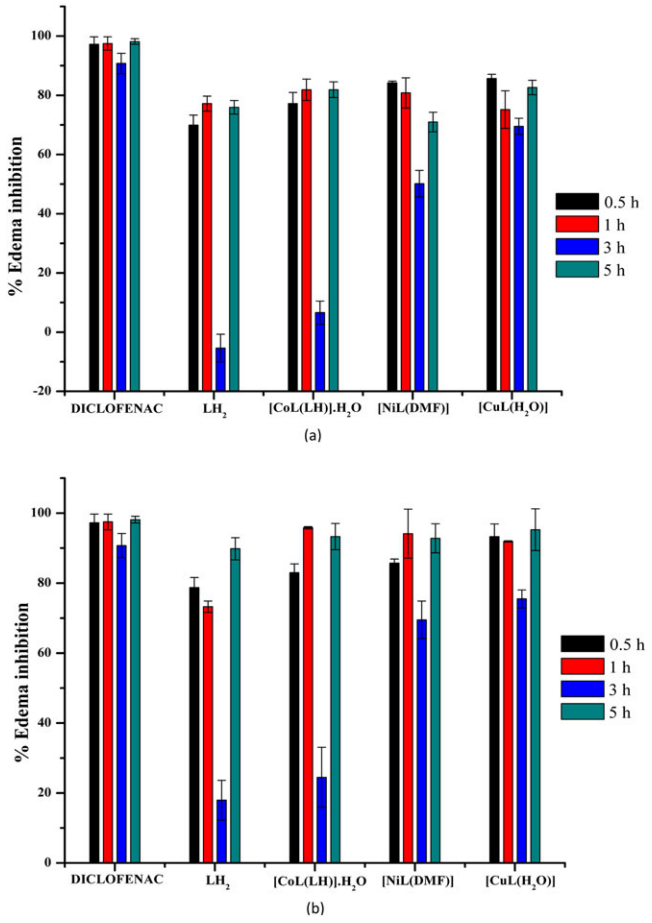

FIGURE 8 Effect of LH_2 and its metal complexes on inhibition of carrageenan-induced rat paw oedema at a dose of (a) 5 mg kg^{-1} and (b) 10 mg kg^{-1}

and Cu(II) complexes were docked at the active sites of COX-2 and 5-LOX proteins, and various interactions have been laid out.

The docked poses in COX-2 protein, displayed in Figure 6, reveal that LH_2 displays hydrogen bond contact with Cys32 amino acid (>N—H···O=C< (amino acid), 2.24 Å). In addition, it forms some weak hydrophobic interactions with Pro139, Leu138, Lys 454, Cys21 and Arg455 amino acids. The most notable interactions were observed in the case of the Co(III) complex with the highest binding affinity of −12.6 kcal mol^{-1} comprising hydrogen bonding interactions with Arg46 amino acid (>N—H···O=C< (amino acid), 2.54 Å) and hydrophobic interactions with Arg29 (π–σ, 3.86 Å) and Tyr108 (π–σ (3.77 Å) and π–π (5.1 Å)). The Ni(II) complex acts as hydrogen bonding acceptor for Asn19 (>C=O···H—N (amino acid), 2.98 Å) and Gln313(C_6H_4 π cloud···H—N(amino acid), 3.24 Å). The carbonyl oxygen of the Cu(II) complex is a classical hydrogen bond acceptor for Asn19 (>C=O···H—N (amino acid), 2.8 Å). In addition, van der Waals interactions with Asp144 (3.7 Å) and weak hydrophobic interactions (4.6–5.0 Å) are observed in the docked model for the Cu(II) complex.

The docked poses in 5-LOX protein, displayed in Figure 7, reveal that LH_2 forms a hydrogen bonding interaction with the protein with 9.3 kcal mol^{-1}. The Co(III) complex exhibited highest binding affinity of −10.8 kcal mol^{-1}, which stems from the excellent five hydrogen bonding contacts made with the protein. The carbonyl oxygens of the amide groups act as hydrogen bond acceptors for Arg246 (>C=O···H—N< (amino acid), 1.84–2.45 Å) and hydrogen bond donors for Glu287 (>N—H···O=C< (amino acid), 2.83 Å). The higher affinity of the Co(III) complex is attributed to the octahedral structure. The Ni(II) and Cu(II) complexes show binding affinity of −9.6 and

TABLE 6 Anti-inflammatory activity of LH_2 and its metal complexes[a]

	Paw volume in ml (% oedema inhibition)			
Groups	**0.5 h**	**1 h**	**3 h**	**5 h**
Control	1.097±0.044	1.197±0.014	1.170±0.062	1.343±0.028
Diclofenac (10 mg kg^{-1})	0.030±0.027*** (97.27%)	0.030±0.027*** (97.49%)	0.108±0.040*** (90.74%)	0.025±0.013*** (98.14%)
LH_2 (5 mg kg^{-1})	0.330±0.037*** (69.92%)	0.273±0.030*** (77.19%)	1.233±0.055 (5.38%)	0.323±0.031*** (75.93%)
LH_2 (10 mg kg^{-1})	0.233±0.031*** (78.73%)	0.320±0.019*** (73.27%)	0.960±0.066 (17.95%)	0.137±0.042*** (89.82%)
$[Co(L)(LH)]\cdot H_2O$ (5 mg kg^{-1})	0.157±0.015*** (85.69%)	0.297±0.076*** (75.19%)	0.357±0.032*** (69.51%)	0.233±0.033*** (82.63%)
$[Co(L)(LH)]\cdot H_2O$ (10 mg kg^{-1})	0.073±0.039*** (93.32%)	0.097±0.002*** (91.92%)	0.287±0.030*** (75.50%)	0.063±0.080*** (95.28%)
[Ni(L)(DMF)] (5 mg kg^{-1})	0.173±0.006*** (84.23%)	0.230±0.061*** (80.79%)	0.583±0.052*** (50.15%)	0.390±0.044*** (70.96%)
[Ni(L)(DMF)] (10 mg kg^{-1})	0.157±0.013*** (85.72%)	0.070±0.084*** (94.15%)	0.357±0.063*** (69.51%)	0.0967±0.056*** (92.80%)
$[Cu(L)(H_2O)]$ (5 mg kg^{-1})	0.250±0.041*** (84.23%)	0.217±0.043*** (81.87%)	1.093±0.046 (6.58%)	0.243±0.035*** (81.88%)
$[Cu(L)(H_2O)]$ (10 mg kg^{-1})	0.187±0.027*** (82.98%)	0.050±0.004*** (95.82%)	0.883±0.100 (24.50%)	0.090±0.050*** (93.30%)

[a]Results expressed in mean ± SEM ($n = 6$); ANOVA followed by Dunnett's test.

***$p < 0.001$, when compared to control group.

−9.4 kcal mol^{-1}, respectively. The former is in hydrogen bonding contacts with Asn328 (>C=O···H—N (amino acid), 2.50 Å) and the latter forms a non-classical hydrogen bond with Ala453. The molecular docking results lead to the conclusion that LH_2 and its complexes effectively bind to the proteins which substantiate the observed activity with the Co(III) complex showing the highest tendency towards protein binding. Molecular docking results of all the synthesized anti-inflammatory models are listed in Table 5.

3.9 | Anti-inflammatory Activity

All the synthesized compounds were screened for their *in vivo* anti-inflammatory activity using the carrageenan-induced rat paw oedema model which is a well-known model of acute inflammation that includes biphasic phases and a number of mediators participate in the inflammatory response evoked by carrageenan.[54] The early phase of the inflammatory response is presumably mediated by the release of histamine and 5-hydroxytryptamine for 90 min followed by the kinin-mediated increased vascular permeability up to 2.5 h. The later phase involves neutrophil infiltration and the release of prostaglandins and prostaglandin-associated leukocytes into the site of oedema[55]; thus the feet rapidly became swollen, reaching close to the control's level by 3.5 h. The experimental results demonstrated that LH_2 and its metal complexes significantly reduced both phases of the carrageenan-induced oedema (Figure 8). Comparison of LH_2 with its complexes indicates that the metal complexes exhibit better activity than the ligand itself. This is due to the increased lipophilic nature of the complexes.[56,57] Among the complexes, $[Co(L)(LH)]\cdot H_2O$ exhibited significant inhibition of paw oedema (95.5%) at a concentration of 10 mg kg^{-1}. Anti-inflammatory activity of the synthesized metal complexes is greater as compared to corresponding metal salts. The results indicating oedema volume and percentage inhibition of inflammation of synthesized compounds and metal salts at various time intervals are summarized in Table 6 and Table S1, respectively.

4 | CONCLUSIONS

A new *ONO* tridentate hydrazone (LH_2) and its Co(III), Ni(II) and Cu(II) complexes were synthesized and characterized. In $[Co(L)(LH)]\cdot H_2O$ both the tautomeric forms of LH_2 are associated with the metal. The acetate ion bestowed the desired basic medium to stabilize both tautomeric forms, resulting in a neutral distorted octahedral Co(III) complex. While in the Ni(II) and Cu(II) complexes, ligand coordinates to metal through imidol tautomeric form resulting in distorted square planar geometry. HS analysis was undertaken to explore the detailed intermolecular contacts. Fingerprint plots generated from HSs are employed for analysing and comparing intermolecular interactions. *In vivo* anti-inflammatory activities of the free ligand and the complexes revealed that complexation enhanced the anti-inflammatory potency of the ligand. Molecular docking analyses of the compounds with COX-2 and 5-LOX proteins demonstrated a good fit of these compounds in both the protein cavities. The Co(III) complex showed a best fit pose in the protein cavities with the lowest binding energy of −12.6 (in COX-2) and −10.8 kcal mol^{-1} (in 5-LOX). The results of docking studies strongly correlate with *in vivo* anti-inflammatory activity results.

ACKNOWLEDGEMENTS

The authors thank USIC, Karnatak University, Dharwad for IR and electronic spectral analyses, CDRI Lucknow for ESI mass analysis, and Indian Institute of Science, Bangalore and IIT Bombay for recording NMR and ESR spectra. The authors sincerely acknowledge the financial support of UGC, New Delhi under UPE-FAR-I Program (no. 14-3/2012). One of the authors (G.H.C.) is grateful to UGC for awarding a RFSMS fellowship.

ORCID

Kalagouda B. Gudasi http://orcid.org/0000-0002-0063-7656

REFERENCES

[1] J. Claria, M. Romano, *Curr. Pharm. Des.* **2005**, *11*, 3431.

[2] D. B. Reddy, T. C. M. Reddy, G. Jyotsna, S. Sharan, N. Priya, V. Lakshmipathi, P. Reddanna, *J. Ethnopharmacol.* **2009**, *124*, 506.

[3] A. S. Michaelidou, D. Hadjipavlou-Litina, *Chem. Rev.* **2005**, *105*, 3235.

[4] B. R. da Costa, S. Reichenbach, N. Keller, L. Nartey, S. Wandel, P. Juni, S. Trelle, *Lancet* **2017**, *390*, 21.

[5] J. Z. Haeggström, A. Rinaldo-Matthis, C. E. Wheelock, A. Wetterholm, *Biochem. Biophys. Res. Commun.* **2010**, *396*, 135.

[6] J. M. Janusz, P. A. Young, J. M. Ridgeway, M. W. Scherz, K. Enzweiler, L. I. Wu, L. Gan, J. Chen, D. E. Kellstein, S. A. Green, J. L. Tulich, T. Rosario-Jansen, I. Jack Magrisso, K. R. Wehmeyer, D. L. Kuhlenbeck, T. H. Eichhold, R. L. M. Dobson, *J. Med. Chem.* **1998**, *41*, 3515.

[7] C. Charlier, C. Michaux, *Eur. J. Med. Chem.* **2003**, *38*, 645.

[8] U. Kendur, G. H. Chimmalagi, S. M. Patil, K. B. Gudasi, C. S. Frampton, C. V. Mangannavar, I. S. Muchchandi, *J. Mol. Struct.* **2018**, *1153*, 299.

[9] Y. Li, Z. Yang, M. Zhou, J. He, X. Wang, Y. Wu, Z. Wang, *J. Mol. Struct.* **2017**, *1130*, 818.

[10] M. Sutradhar, M. V. Kirillova, M. Fátima, C. Guedes da Silva, C. Liuc, A. J. L. Pombeiro, *Dalton Trans.* **2013**, *42*, 16578.

[11] J. G. Deng, Y. Gou, W. Chen, X. Fu, H. Deng, *Bioorg. Med. Chem.* **2016**, *24*, 2190.

[12] M. Sutradhar, E. C. B. A. Alegria, K. T. Mahmudov, M. Fatima, C. Guedes da Silva, A. J. L. Pombeiro, *RSC Adv.* **2016**, *6*, 8079.

[13] W. B. Junior, M. S. Alexandre-Moreira, M. A. Alves, A. Perez-Rebolledo, G. L. Parrilha, E. E. Castellano, O. E. Piro, E. J. Barreiro, L. Lima, H. Beraldo, *Molecules* **2011**, *16*, 6902.

[14] R. P. Bakale, G. N. Naik, C. V. Mangannavar, I. S. Muchchandi, I. N. Shcherbakov, C. Frampton, K. B. Gudasi, *Eur. J. Med. Chem.* **2014**, *73*, 38.

[15] S. Y. Ebrahimipour, I. Sheikhshoaie, J. Simpson, H. Ebrahimnejad, M. Dusek, N. Kharazmi, V. Eigner, *New J. Chem.* **2016**, *40*, 2401.

[16] R. S. Hunoor, B. R. Patil, D. S. Badiger, V. M. Chandrashekhar, I. S. Muchchandi, K. B. Gudasi, *Appl. Organometal. Chem.* **2015**, *29*, 101.

[17] R. S. Hunoor, B. R. Patil, D. S. Badiger, R. S. Vadavi, K. B. Gudasi, V. M. Chandrashekhar, I. S. Muchchandi, *Spectrochim. Acta Mol.* **2010**, *77*, 838.

[18] M. Saif, H. F. El-Shafiy, M. M. Mashaly, M. F. Eid, A. I. Nabeel, R. Fouad, *J. Mol. Struct.* **2016**, *111*, 875.

[19] K. K. Varsha, L. Devendra, G. Shilpa, S. Priya, A. Pandey, K. M. Nampoothiri, *Int. J. Food Microbiol.* **2015**, *211*, 44.

[20] J. M. Janusz, P. A. Young, J. M. Ridgeway, M. W. Scherz, K. Enzweiler, L. I. Wu, L. Gan, R. Darolia, R. S. Matthews, D. Hennes, D. E. Kellstein, S. A. Green, J. L. Tulich, T. Rosario-Jansen, I. Jack Magrisso, K. R. Wehmeyer, D. L. Kuhlenbeck, T. H. Eichhold, R. L. M. Dobson, S. P. Sirko, R. W. Farmer, *J. Med. Chem.* **1998**, *41*, 1112.

[21] S. Ghatak, A. Vyas, S. Misra, P. O'Brien, A. Zambre, V. M. Fresco, R. R. Markwald, K. Venkateshwara Swamy, Z. Afrasiabi, A. Choudhury, M. Khetmalas, S. Padhye, *Bioorg. Med. Chem. Lett.* **2014**, *24*, 317.

[22] D. S. Badiger, R. B. Nidavani, R. S. Hunoor, B. R. Patil, R. S. Vadavi, V. M. Chandrashekhar, I. S. Muchchandi, K. B. Gudasi, *Appl. Organometal. Chem.* **2011**, *25*, 876.

[23] M. Nath, P. Saini, A. Kumar, *Appl. Organometal. Chem.* **2009**, *23*, 434.

[24] Z. H. Chohan, M. S. Iqbal, H. S. Iqbal, A. Scozzafava, C. T. Supuran, *J. Enzyme Inhib. Med. Chem.* **2002**, *17*, 87.

[25] F. Dimiza, A. N. Papadopoulos, V. Tangoulis, V. Psycharis, C. P. Raptopoulou, D. P. Kessissoglou, G. Psomas, *Dalton Trans.* **2010**, *39*, 4517.

[26] A. I. Vogel, *A Textbook of Quantitative Inorganic Analysis*, 3rd ed., Longmans Green and Co. Ltd, London **1961**.

[27] CrysAlisPRO software system, *Version 1.171.38.41, Rigaku Oxford Diffraction*, Rigaku Corporation, Oxford **2015**.

[28] G. Sheldrick, *Acta Crystallogr. C* **2015**, *71*, 3.

[29] C. F. Macrae, I. J. Bruno, J. A. Chisholm, P. R. Edgington, P. McCabe, E. Pidcock, L. Rodriguez-Monge, R. Taylor, J. van de Streek, P. A. Wood, *J. Appl. Crystallogr.* **2008**, *41*, 466.

[30] D. J. Grimwood, S. K. Wolff, J. J. McKinnon, M. J. Turner, D. Jayatilaka, M. A. Spackman, *CrystalExplorer* **2013**, *3*, 1.

[31] S. Seth, *J. Mol. Struct.* **2016**, *1118*, 75.

[32] M. Atzori, L. Marchiò, R. Clérac, A. Serpe, P. Deplano, N. Avarvari, M. L. Mercuri, *Cryst. Growth Des.* **2014**, *14*, 5938.

[33] Y. Li, Y. Luo, J. Wang, C. Chen, B. Sun, *J. Mol. Struct.* **2018**, *1153*, 96.

[34] O. Trott, A. J. Olson, *J. Comput. Chem.* **2010**, *31*, 455.

[35] F. Neese, *Wiley Interdiscip. Rev. Comput. Mol. Sci.* **2012**, *2*, 73.

[36] A. Schafer, C. Huber, R. Ahlrichs, *J. Chem. Phys.* **1994**, *100*, 5829.

[37] M. D. Hanwell, D. E. Curtis, D. C. Lonie, T. Vandermeersch, E. Zurek, G. R. Hutchison, *Aust. J. Chem.* **2012**, *4*, 1.

[38] M. F. Sanner, *J. Mol. Graphics Modell.* **1999**, *17*, 57.

[39] M. Ulusoy, H. Karabıyık, R. Kılınçarslan, M. Aygün, B. Çetinkaya, S. García-Granda, *Struct. Chem.* **2008**, *19*, 749.

[40] Y. Li, Y. Luo, J. Wang, C. Chen, B. Sun, *J. Biomater. Sci. Polym. Ed.* **2017**, *1*.

[41] S. Mondal, B. Pakhira, A. J. Blake, M. G. B. Drew, S. Chattopadhyay, *Polyhedron* **2016**, *117*, 327.

[42] F. Dreiocker, J. Oomens, A. J. H. M. Meijer, B. T. Pickup, R. F. W. Jackson, M. Schafer, *J. Org. Chem.* **2010**, *75*, 1203.

[43] J. Figuerasp, P. W. Scullardan, A. R. Mack, *J. Org. Chem.* **1971**, *36*, 3497.

[44] J. B. Gandhi, N. D. Kulkarni, *Transition Met. Chem.* **2000**, *25*, 209.

[45] A. B. P. Lever, *Inorganic Electronic Spectroscopy*, Elsevier, Amsterdam **1984** 553.

[46] S. Chandra, K. B. Pandeya, R. P. Singh, *Indian J. Chem.* **1979**, *18A*, 476.

[47] U. Sakaguchi, A. W. Addison, *J. Chem. Soc. Dalton Trans.* **1979**, *4*, 600.

[48] B. J. Hathaway, D. E. Billing, *Coord. Chem. Rev.* **1970**, *5*, 143.

[49] M. M. Sow, O. Diouf, M. Gaye, A. S. Sall, P. Perez-Lourido, L. Valencia-Matarranz, G. Castro, A. Canesch, L. Sorace, *Inorg. Chim. Acta* **2013**, *406*, 171.

[50] R. Karmakar, C. Roy Choudhury, A. S. Batsanov, S. R. Batten, S. Mitra, *Struct. Chem.* **2005**, *16*, 535.

[51] J. J. McKinnon, A. S. Mitchell, M. A. Spackman, *Acta Crystallogr. B* **2004**, *60*, 627.

[52] S. Seth, N. Saha, S. Ghosh, T. Kar, *Chem. Phys. Lett.* **2011**, *506*, 309.

[53] A. D. Martin, K. J. Hartlieb, A. N. Sobolev, C. L. Raston, *Cryst. Growth Des.* **2010**, *10*, 5302.

[54] M. Di Rosa, J. P. Giroud, D. A. Willouchby, *J. Pathol.* **1971**, *104*, 15.

[55] E. Ricciotti, G. A. FitzGerald, *Arterioscler., Thromb., Vasc. Biol.* **2011**, *31*, 986.

[56] M. Konstandinidou, A. Kourounakis, M. Yiangou, L. Hadjipetrou, D. Kovala-Demertzi, S. Hadjikakou, M. Demertzis, *J. Inorg. Biochem.* **1998**, *70*, 63.

[57] M. Roch-Arveiller, D. Pham Huy, L. Maman, J. Giroud, J. R. J. Sorenson, *Biochem. Pharmacol.* **1990**, *3*, 569.

SUPPORTING INFORMATION

Additional Supporting Information may be found online in the supporting information tab for this article.

How to cite this article: Chimmalagi GH, Kendur U, Patil SM, et al. Mononuclear Co(III), Ni(II) and Cu(II) complexes of tridentate di-*tert*-butylphenylhydrazone: Synthesis, characterization, X-ray crystal structures, Hirshfeld surface analysis, molecular docking and *in vivo* anti-inflammatory activity. *Appl Organometal Chem*. 2018;e4337. https://doi.org/10.1002/aoc.4337